CrystEngComm



PAPER



Cite this: CrystEngComm, 2022, 24, 8399

Metal-organic framework induced hybrid NiCo₂S₄/PPy structures with unique interface features for high performance flexible energy storage devices

He Huang,^a Lihua Miao, ¹

**Dan Yang,^a Baoping Kuang^a and Chaohui Zhang^a

Received 20th August 2022, Accepted 2nd November 2022

DOI: 10.1039/d2ce01142e

rsc.li/crystengcomm

Designing electrodes with hybrid structures is significant for improving energy storage devices. Overall, single-component metal oxides usually show poor stability and conductivity. In order to solve this problem, based on the easy-to-modify properties of spinel-structured NiCo₂S₄, hybrid-structure NiCo₂S₄/PPy is successfully synthesized through hydrothermal synthesis and electrodeposition methods, and uniformly grown on nickel foam. Hybrid NiCo₂S₄/PPy structures exhibit a high specific capacitance of 983 C g⁻¹ at 1 A g⁻¹ and excellent stability. The assembled supercapacitor device reaches a high energy density of 76.5 W kg⁻¹ at 2984 W h kg⁻¹ and excellent cycling performance, and mechanical flexibility.

Introduction

Nowadays, with the increasing demand for sustainable renewable energy, research on energy storage devices is a hot topic in today's society. 1-3 Supercapacitors have attracted the attention of a wide range of researchers due to their advantages such as fast charging and discharging capability and higher power density. 4-6 However, the low energy density is the main factor limiting the further application of supercapacitors, and the energy density is affected by the electrochemical activity, microstructure, electrical conductivity, specific surface area, etc. of the supercapacitors.^{7,8} In addition, it is well known that supercapacitors presents lots of the inherent characteristics.9 Therefore, the research focus of supercapacitors is to develop electrode materials with excellent electrochemical properties. Transition metal sulphides are receiving increasing attention as an important pseudocapacitive material due to their higher electrical conductivity (about 104 times), lower band gap energy and better structural stability compared to oxides. 10-12 Compared with single metal sulfides, mixed metal sulfides (MMS) exhibit higher electronic conductivity, thereby significantly improving electrochemical performance, making it the best electrode material candidate for supercapacitors.¹³ However, the brittle crystal structure of transition metal sulfides tends to collapse during long-term cycling, which further reduces the cycling stability and hinders their practical application.

Rational design of the electrode material structure is an effective strategy to improve the electrochemical kinetics. 14,15 Metal-organic frameworks (MOFs) have attracted much interest in the energy field due to their unique crystal structure, large specific surface area and high porosity. 16 Zhao et al. synthesized Ni-Co-S nanosheets on carbon cloth by etching and ion exchange methods. The electrode material obtained a specific capacitance of 2392 F g⁻¹ at a current density of 1 A g⁻¹, and the assembled flexible device had an energy density of 30.2 W h kg⁻¹ at a power density of 800.2 W kg⁻¹.¹⁷ Wan and his co-workers synthesized Ni-Mn-S@NiCo₂S₄ core-shell heterostructures through a two-step electrodeposition method. Due to their unique structure and the synergistic effect of different components, a high specific capacity of 939.0 C g⁻¹ can be achieved at a current density of 1 A g⁻¹, and a long cycle life with a loss of only 9.7% after 5000 cycles at 5 A g⁻¹ can be achieved. The assembled asymmetric device provides a high energy density of 59.1 W h kg⁻¹ at a power density of 344.8 W kg⁻¹. ¹⁸ Although the porous structure of MOFs and their diverse chemical properties make them popular, their poor electrical conductivity seriously affects the electrochemical performance of electrode materials. The core-shell structure has been reported to be effective in improving the electrochemical performance of electrode materials. PPy is widely used as a pseudocapacitor material for supercapacitors due to its excellent electrical conductivity and good cycling performance. 19,20 Guo's team prepared unique PPy@NiCo2S4 core-shell heterostructured materials with large specific surface area and obtained a specific capacitance of 908.1 F g⁻¹ at a current density of 1 A g-1. The asymmetric supercapacitor provides a high energy density of over 50.82 W h kg⁻¹ and a high power density of 160 W kg⁻¹.21

^a School of Medical Information Engineering, Shenyang Medical College, Shenyang 110034, Liaoning, China. E-mail: miaolihua@163.com

^b School of pharmacy, Shenyang Medical College, Shenyang, 110043, Liaoning, China

In this work, hybrid structured NiCo₂S₄/PPy is obtained through a two-step method. The prepared NiCo₂S₄@PPy-110 material presents excellent electrochemical performance with a specific capacity of 983 C g⁻¹ at 1 A g⁻¹ and 86.7% capacitance retention after 10000 cycles. Finally, the assembled device presents an energy density of 76.5 W h kg⁻¹ at a power density of 2984 W kg⁻¹. This work provides the design of ultra-fine nanoarrays and contributes to the preparation of hybrid structures for the next generation of energy storage devices.

Experimental section

Preparation of Co-MOF

First, all reagents can be used directly without further processing. In a typical step, 0.291 g $Co(NO_3)_2 \cdot 6H_2O$ and 0.8 g 2-methylimidazole were dissolved in 30 mL of deionized water and stirred for 10 min, respectively. The 2-methylimidazole solution and the pre-treated Ni foam were rapidly injected into the cobalt nitrate for 10 minutes, then washed three times with ethanol and deionized water, and dried at 60 °C overnight.

Preparation of the Ni-Co precursor

The previously prepared Co-MOF was dipped into 60 mL of deionized water containing 0.145 g Ni(NO₃)₂·6H₂O, transferred to a 100 mL autoclave, and kept at 90 °C for 1 h to prepare the Ni–Co precursor.

Preparation of NiCo₂S₄ nanosheets

0.4804 g $Na_2S\cdot 9H_2O$ was dissolved in 60 mL deionized water and stirred for 10 minutes, then the previously prepared Ni–Co precursor was immersed into it and transferred to an autoclave, and heated at 120 °C for 4 h to finally obtain the $NiCo_2S_4$ sample. The average mass loading is 1.0 mg cm⁻².

Preparation of hybrid structured NiCo₂S₄@PPy nanosheets

First, the prepared $\rm NiCo_2S_4$ sample was used as the working electrode, Ag/AgCl as the reference electrode and Pt sheet as the counter electrode under the three-electrode system. 1 g of p-toluenesulfonic acid and 2 mL of pyrrole were dissolved in 100 mL of deionized water as the electrolyte and deposited at 0.8 V for 70, 110, and 150 s, respectively. The average mass loading is 1.1, 1.31, and 1.46 mg cm $^{-2}$, respectively.

Materials characterization

X-ray diffraction (XRD, 7000, Shimadzu, 40 kV, Cu K α , λ = 0.1541 nm), scanning electron microscopy (SEM; Gemini SEM 300-71-31) and transmission electron microscopy (TEM, JEM-2100 PLUS) are used to analyze the microstructure the prepared products. The elemental composition of the synthesized samples was obtained by X-ray photoelectron spectrometry (XPS, ESCALAB 250 Xi, Thermo scientific).

Electrochemical measurements

Electrochemical performance testing is performed using a CHI660E electrochemical workstation. Cyclic voltammetry (CV), constant current charging/discharging (GCD) and electrochemical impedance spectroscopy (EIS) were performed with synthetic products as the working electrode, Hg/HgO as the reference electrode and platinum sheets as the counter electrode in 3 M KOH electrolyte. The mass capacitance (*C*), energy density (*E*) and power density (*P*) of the product can be obtained by the following equations:

$$C = I\Delta t/m \tag{1}$$

$$E = 1/2CV^2 \tag{2}$$

$$P = 3600E/\Delta t \tag{3}$$

where I represents the discharge current, Δt is the discharge time, m is the mass loading of the prepared sample, and V is the voltage window.

Assembly of asymmetric supercapacitors

The active carbon (AC) electrode was used as the negative electrode, NiCo $_2$ S $_4$ /PPy is used as the positive electrode, PVA–KOH is used as the electrolyte, and NiCo $_2$ S $_4$ /PPy is used as the positive electrode. Electrolyte preparation: 3 g KOH and 3 g PVA were placed in 30 ml DI water, and the mixture was maintained at 80 °C in a water bath and stirred for 1 h until the solution was clear and could be reserved for later use. Preparation of activated carbon: activated carbon, acetylene black and polyvinylidene fluoride were used as raw materials, according to a mass ratio of 7:2:1, and the mixture was coated on the surface of Ni foam, and dried at 60 °C for 24 hours.

Results and discussion

The hybrid NiCo₂S₄/PPy structure is constructed by facile hydrothermal reactions followed by electrodeposition as shown in Fig. 1. Firstly, Co-MOF was obtained at a room temperature. Next, the NiCo precursor was obtained by the ion exchange method at room temperature. Secondly, nanosheet-like NiCo₂S₄ precursors are synthesized on the nickel foam through the vulcanization method. Finally, PPy nanosheets were electrodeposited on the surface of NiCo₂S₄ samples.

Fig. 1a shows the XRD patterns of the as-fabricated products. Three high-intensity diffraction peaks at 2θ angles of 44.4° , 51.6° and 76.1° can be attributed to nickel foam. The diffraction peaks located at 2θ values of 31.6° , 38.3° , 50.5° , 55.3° and 65.1° could be identified as the (311), (400), (511), (440) and (533) crystal planes of cubic phase NiCo₂S₄ (JCPDs card no. 20-0782), respectively. There are no characteristic peaks of other impurities, indicating that hybrid products possess high purity. To confirm that PPy is successfully grown on the surface of the samples,

CrystEngComm Paper

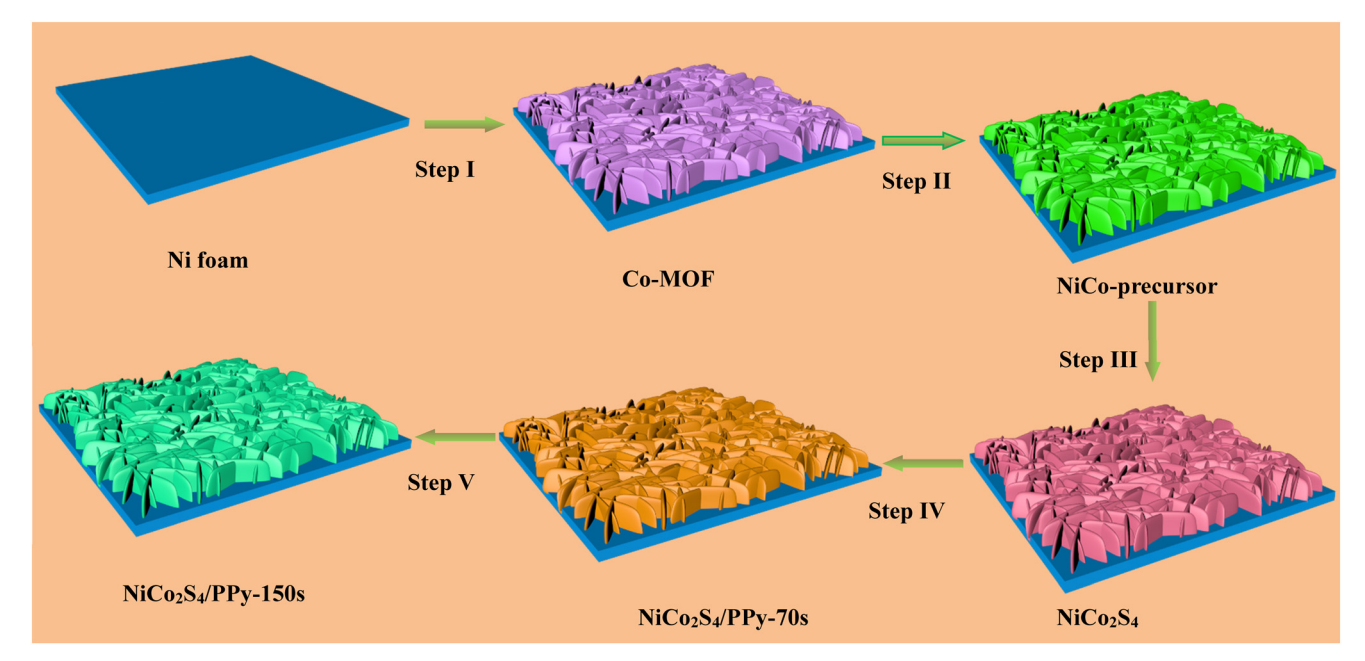


Fig. 1 Synthesis schematic of the hybrid NiCo₂S₄/PPy structure.

corresponding XPS tests are performed, as depicted in Fig. 1b. It can found that four elements, Ni, Co, S and N, exist on the whole sample, demonstrating that hybrid NiCo₂-S₄/PPy structures are successfully prepared. Ni 2p (Fig. 1c) can be fitted with two main peaks at 852.4 and 869.2 eV which are assigned to Ni 2p_{3/2} and Ni 2p_{1/2}, respectively. 22,23

The peaks at 858.2 and 875.8 eV belong to spin-orbit doublets. 24,25 As shown in Fig. 1d, the Co $2p_{3/2}$ and Co $2p_{1/2}$ of the sulfides are located at 781.6 and 797.5 eV. In the fitted peaks, 798.5 and 782.5 eV can be attributed to Co^{2^+} , and 797.4 and 781.4 eV can be assigned to Co^{3^+} . As shown in Fig. 1e, the peaks located at 168.9, 163.7 eV and 162.4 eV

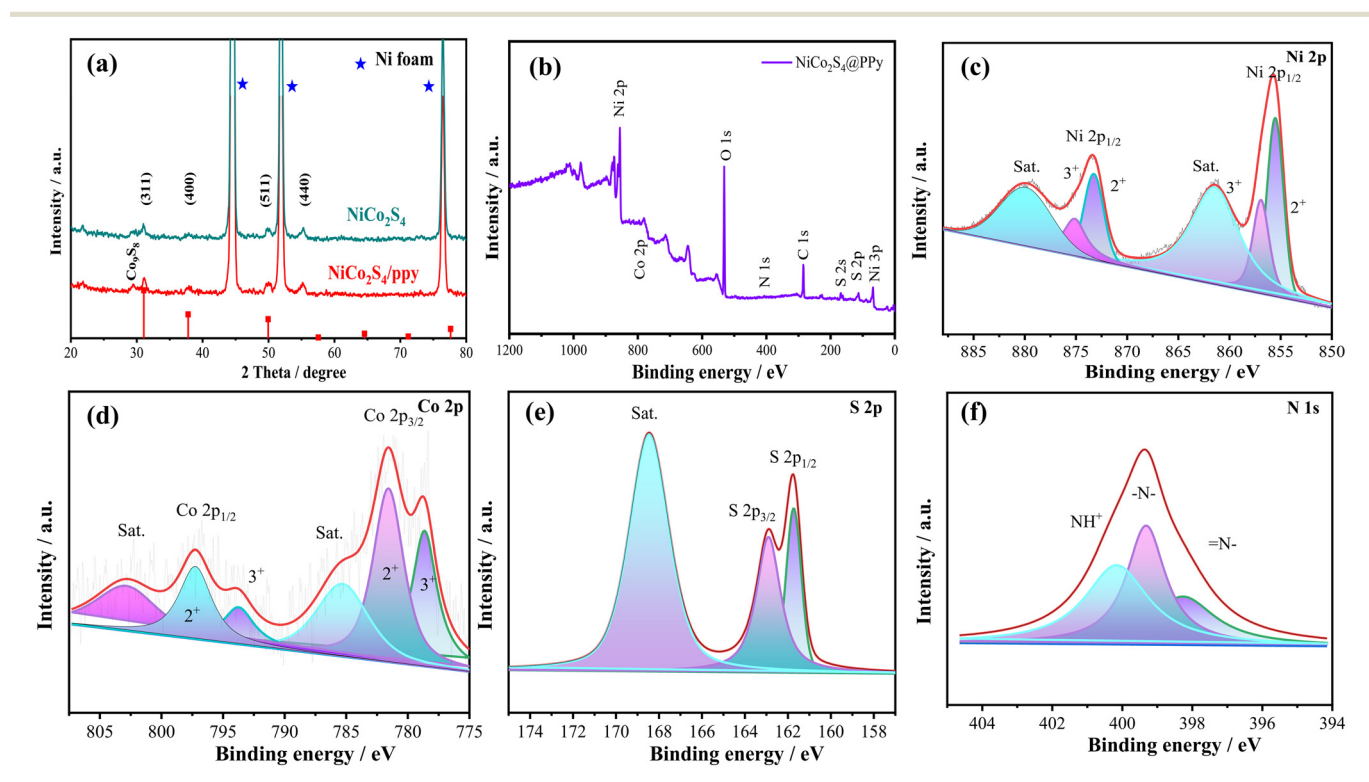


Fig. 2 Structure characterization of the samples. (a) XRD patterns of $NiCo_2S_4$ and $NiCo_2S_4$ /PPy; XPS full spectrum of (b) $NiCo_2S_4$ /PPy, (c) Ni 2p, (d) $NiCo_2S_4$ and $NiCo_2S_4$

correspond to the satellite peak, S $2p_{1/2}$ and S $2p_{3/2}$, respectively.^{28,29} The typical peak of the metal–sulfur bond at 162.4 eV can effectively improve the electrochemical activity. Fig. 1f presents N 1s spectra. It can be divided into three typical peaks for PPy. Binding energies at 396.7 eV, 397.5 eV and 401.9 eV correspond to –NH–, –NH⁺– and –N⁺ = cations, respectively (Fig. 2).³⁰

The morphological evolution from Co-MOF nanosheet arrays to $NiCo_2S_4$ @PPy nanosheets was examined by SEM. The SEM image in Fig. 3a shows that the Co-MOF nanosheet array is uniformly covered on the nickel foam, and the average thickness of the nanosheets is about 300 nm. As shown in Fig. 3b, after the reaction with $Ni(NO_3)_2 \cdot 6H_2O$, the structure of the product still keeps growing vertically, but the nanosheet array of the sample becomes thinner due to the etching effect. Fig. 3c shows the SEM images after PPy coating for electrodeposition of 70 s, and the structure of the sample is composed of porous arrays of nanosheets compared to the Ni–Co precursor, which may be caused by

the gas released during the decomposition of the MOF. At the same time, the average thickness of the nanosheets is 40 nm. Fig. 3d shows the SEM image of NiCo2S4/PPy-110, and the thickness of the nanosheet significantly increases (about 45 nm). When the deposition time is 150 s (Fig. 3e), it can be found that the thickness of the nanosheet is about 50 nm at most. The structural information of the NiCo₂S₄/PPy-110 (NCS-110) sample is further analyzed by TEM. As shown in Fig. 3f, ultra-thin nanosheets are coated on the surface of the samples. In Fig. 3g, the interplanar spacing is 0.24 nm, which is attributed to the (400) plane of the NiCo₂S₄ phase. This is consistent with the XRD results. In addition, the selected area electron diffraction (SAED, Fig. 3h) pattern indicates several rings due to the polycrystalline structure. In Fig. 3i, EDS mapping of as-prepared samples indicate that four elements, Ni, Co, S and N, are uniformly distributed on the whole surface of the materials.

The electrochemical properties of the synthesized products were tested under a three-electrode system. The CV

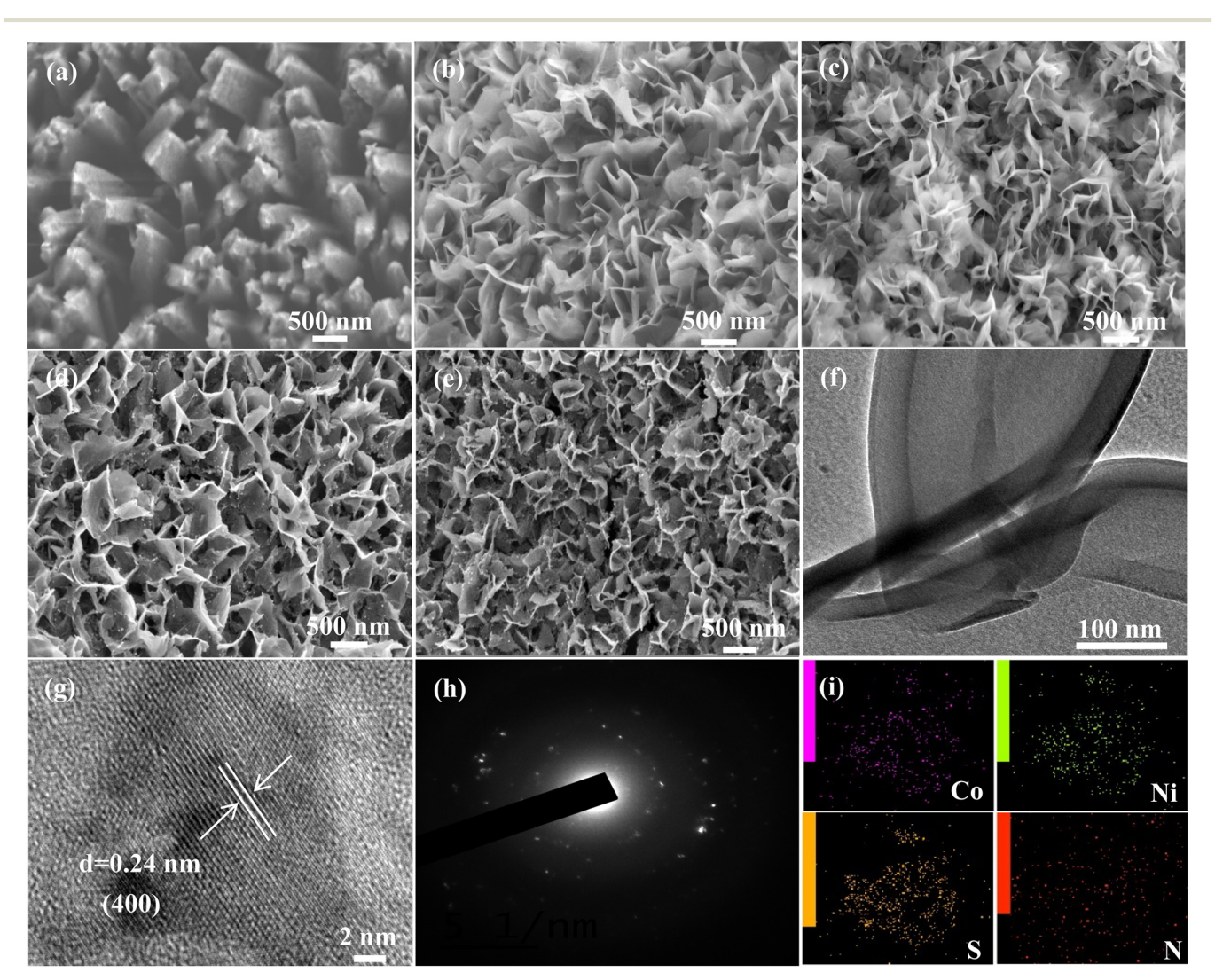


Fig. 3 SEM and TEM images of (a) Co-MOF, (b) NiCo₂S₄/PPy-10 structure, (d) NiCo₂S₄/PPy-110 structure, (e) NiCo₂S₄/PPy-150 structure and (f and g) NiCo₂S₄/PPy-110 structure; (h) SAED pattern and (i) elemental mapping.

CrystEngComm Paper

curves of NCS-70, NCS-110, NCS-150 and NiCo2S4 electrode materials at a sweep rate of 50 mV s⁻¹ are shown in Fig. 4a. Compared with other electrode materials, the closed area formed by the CV curve of the NCS-110 electrode is the largest at the same sweep speed, indicating its excellent charge storage capacity. Fig. 4b shows the GCD curves of these samples at 1 A g⁻¹. It is clear that the discharge time of the NCS-110 product is longer than that of several other products, implying that the NCS-110 sample has a higher specific capacitance. The CV curves for the NCS-110 product tested at sweep rates from 5 to 50 mV s⁻¹ are shown in Fig. 4c. With the increase of the sweep speed, the shape of the curve remains constant, showing good reversibility, indicating its excellent multiplicative performance. A clear redox peak can be observed in the CV curve, indicating its ideal pseudocapacitance behavior. Fig. 4d shows the GCD curves of the NCS-110 sample at different current densities with a specific capacitance of 1080 C g⁻¹ at 1 A g⁻¹. In order to analyze the reaction kinetics of the electrode materials,

the capacitance contribution can be analyzed by this equation:³¹

$$i = av^b (4)$$

The b value can reflect the relationship of $\log(i)$ and $\log(v)$. From Fig. 4e, NCS-110 and NiCo₂S₄ electrode materials show the b value of 0.61 and 0.58, respectively. Large b value indicates that rapid electron transfer occurs during electrochemical reaction process. The capacitive contribution ratio can be further quantified via following equation:³²

$$i = k_1 \nu + k_2 \nu^{1/2} \tag{5}$$

where i, v, and k_1 and k_2 represent the current, scan rate and constants, respectively. The percentages of capacitance and diffusion are displayed in Fig. 4f. It is found that the contribution of capacitance of the samples increases with the scan rate gradually increasing, indicating that the as-

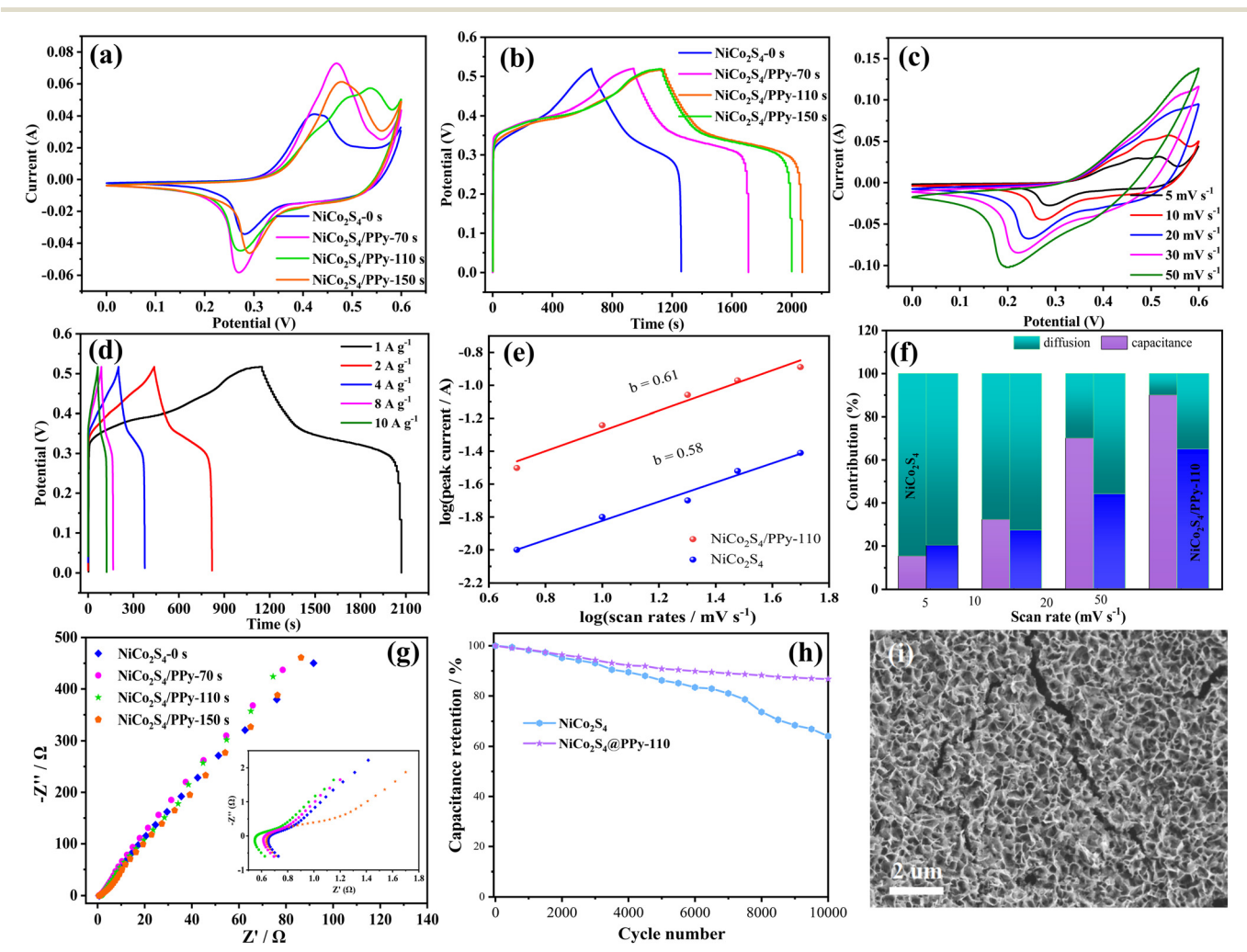


Fig. 4 Electrochemical performance of the as-prepared electrodes. (a) CV curves at 50 mV s⁻¹; (b) GCD curves at 1 A g⁻¹; (c) CV curves of the NiCo₂S₄/PPy-110 structure; (d) charging-discharging curves of the NiCo₂S₄/PPy-110 structure; (e) b-values of the three electrodes; (f) contribution ratio between capacitive (calculated one) and diffusion-controlled capacity; (g) electrochemical impedance plots (inset shows the high-frequency region); (h) cycling stability; (i) SEM images after cycling stability test.

obtained samples can be ascribed to the battery-type electrode materials. From the EIS of all samples (Fig. 4g), the NCS-110 electrode materials show a small R_{ct} of 0.56 Ω , which confirms that the hybrid samples exhibit faster electron transport. In addition, the cycling stability of electrode materials is a key indicator to evaluate the material properties, as presented in Fig. 4h. It is obviously found that the capacitance retention of the NiCo₂S₄ electrode is 64.1% after 10000 cycles. However, the hybrid structured electrode materials present superior cycling stability with a capacitance of 86.7% after 10000 cycles. It can be concluded that a layer of PPy nanosheets on the surface of NiCo2S4 improves the electrical conductivity. In addition, in order to further confirm the stability of the material, the corresponding SEM test was also carried out. SEM showed that the morphology of the prepared samples did not change significantly before and after the cycle.

In order to evaluate the practical application capability of NCS-110 samples, the asymmetric devices were assembled.

Fig. 5a shows the CV curve of the mixed electrode material and activated carbon. It can be seen that the voltage of the device can reach 1.6 V. In order to ensure equal charge between the positive (q^+) and negative (q^-) electrodes $(q = Cm\Delta t)$, the potential and electrode mass (m) of the charging and discharging process should follow the following relation:

$$m^{+}/m^{-} = C_{s}^{-} \times V^{-}/C_{s}^{+} \times V^{+}$$
 (6)

where q^+/q^- (C) is the stored charge of the electrode materials, ΔV (V) represents the potential range, $C_{\rm s}$ is the specific capacitance, and m is the mass loading of the active materials. The mass ratio of the positive electrode and negative electrode is close to 0.41. The CV curve of the device is shown in Fig. 5b. The area of the curve increases with the increase of the scan rate. Fig. 5c shows the CV curves of the device in different voltage windows. It can be found that the shape of the curve remains almost unchanged with the increase of the potential window from 1.1 to 1.5 V. As shown

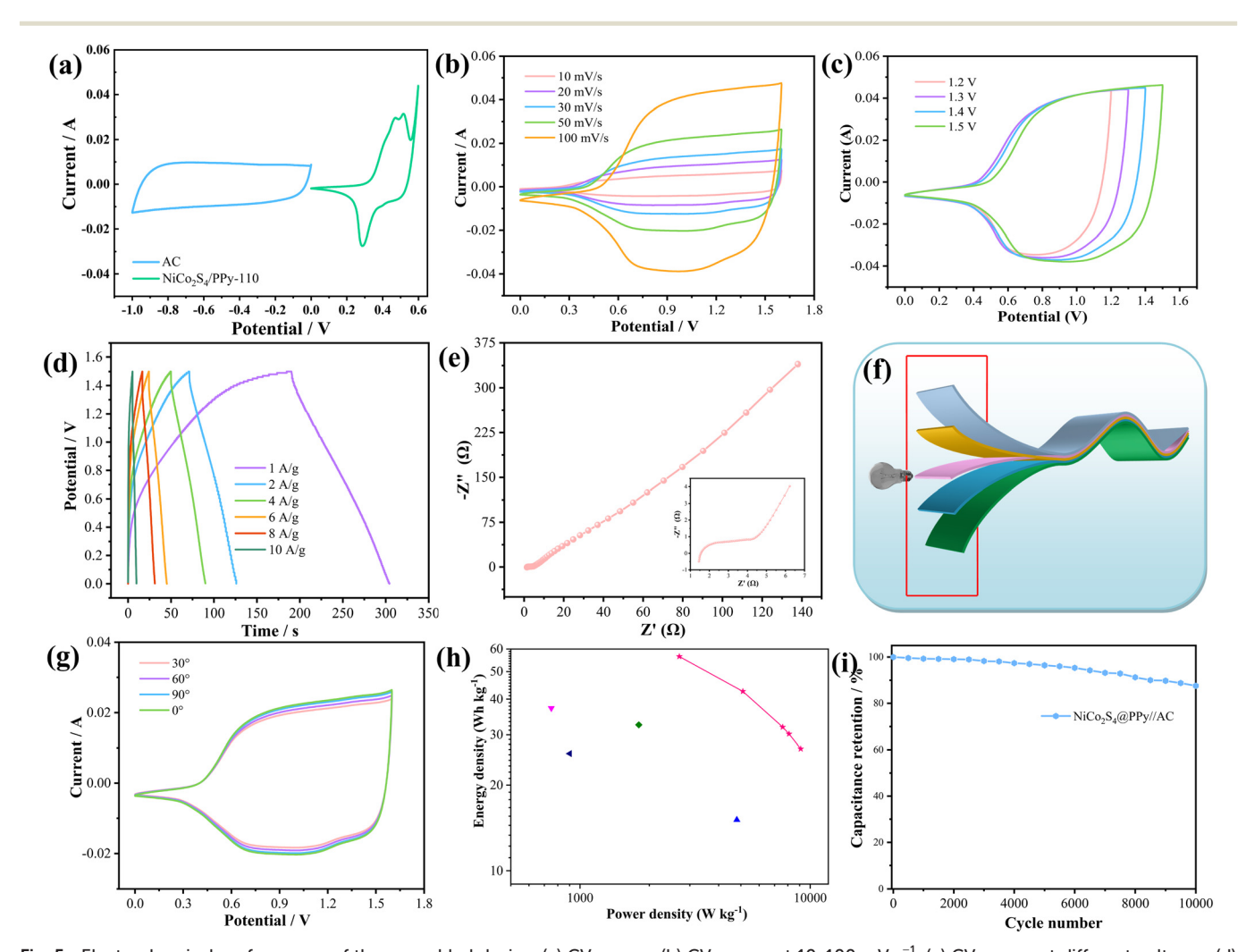


Fig. 5 Electrochemical performance of the assembled device. (a) CV curves, (b) CV curves at $10-100 \text{ mV s}^{-1}$, (c) CV curves at different voltages, (d) GCD curves, (e) Nyquist plots, (f) schematic diagram of the flexible device, (g) CV curves at different bending angles, (h) Ragone plot of the hybrid device and (i) cycling stability.

CrystEngComm Paper

in Fig. 5d, when the current density is 1 A g⁻¹, the discharge time of the device is longer.

The Nyquist plot (Fig. 5e) can be used to analyze the reaction kinetics with EIS, and the frequency range of measurement is 10^{-2} – 10^{5} Hz. It can be intuitively observed that the device is almost straight and does not show a complete semicircle in the whole frequency range. This indicates that the charge transfer resistance (R_{ct}) is low, which is attributed to the farad-type redox reaction promoted by the highly conductive PPy nanosheets. In order to visually understand the resistance relationship, we provide the corresponding fitted circuit with the R_s value of 1.74 Ω for the device, indicating its transcendent conductivity. Next, the superior flexibility of ultrafine nanoarrays can be seen in the schematic of Fig. 5f. This gives great significance to the practical application of flexible and bendable electronics. The CV test was carried out at a sweep speed of 100 mV s⁻¹, and Fig. 5g was obtained. The shape of CV curves at different bending angles did not change significantly, indicating that the performance was almost not affected by bending angles. The energy and power density are shown in the Ragone plot (Fig. 5h). At a power density of 2984 W kg⁻¹, the energy density of the device is 76.5 W h kg⁻¹. Compared with previous devices reported in the literature, this result is superior.^{33–36} The NCS-110 device retained 87.6% of the initial capacitance after 10 000 cycles (Fig. 5i), demonstrating its outstanding long-cycle stability. In conclusion, NCS-110 composite nanoarrays exhibit superior electrochemical performance and excellent potential for flexible energy storage.

Conclusion

In summary, the MOF-derived NiCo₂S₄ electrode material has been successfully obtained by a hydrothermal method, and the corresponding core–shell structured NiCo₂S₄@PPy electrode materials are also prepared by a subsequent electrochemical deposition strategy. Due to the unique structure and highly active sites of the MOF material, the prepared NiCo₂S₄@PPy-110 material presents excellent electrochemical performance with a specific capacity of 983 C g⁻¹ at 1 A g⁻¹ and 86.7% capacitance retention after 10 000 cycles. Finally, the assembled device presents an energy density of 76.5 W h kg⁻¹ at a power density of 2984 W kg⁻¹. This work provides the design of ultra-fine nanoarrays and contributes to the preparation of hybrid structures for the next generation of energy storage devices.

Conflicts of interest

The authors declare no conflict of interest.

Acknowledgements

This project is supported by the Scientific Research Project of Liaoning Provincial Department of Science and Technology (2019-ZD-0333).

References

- 1 Y. H. Wang, R. N. Liu, Y. D. Tian, Z. Sun, Z. H. Huang, X. L. Wu and B. Li, *Chem. Eng. J.*, 2020, **384**, 123263.
- 2 K. F. Chen, F. Liang and D. F. Xue, *Dalton Trans.*, 2020, 49, 1107–1115.
- 3 J. H. Lin, Y. T. Yan, X. H. Zheng, Z. X. Zhong, Y. H. Wang, J. L. Qi, J. Cao, W. D. Fei, Y. D. Huang and J. C. Feng, J. Colloid Interface Sci., 2019, 536, 456-462.
- 4 M. F. El-Kady, V. Strong, S. Dubin and R. B. Kaner, *Science*, 2012, 335, 1326–1330.
- 5 B. Liu, S. Sun, R. Y. Jia, H. S. Zhang, X. H. Zhu, C. G. Zhang, J. Xu, T. Zhai and H. Xia, Adv. Funct. Mater., 2020, 30, 1909546.
- 6 Q. Y. Gui, L. X. Wu, Y. Y. Li and J. P. Liu, Adv. Sci., 2019, 6, 1802067.
- 7 Y. Q. Jiang and J. P. Liu, Energy Environ. Mater., 2019, 2, 30–37.
- 8 G. Xu, J. Han, B. Ding, P. Nie, J. Pan, H. Dou, H. S. Li and X. G. Zhang, *Green Chem.*, 2015, 17, 1668–1674.
- L. Ma, X. P. Shen, Z. Y. Ji, G. X. Zhu and H. Zhou, *Chem. Eng. J.*, 2014, 252, 95–103.
- 10 L. Chen, X. T. Xu, L. J. Wan, G. Zhu, Y. J. Li, T. Lu, M. D. Albaqami, L. K. Pan and Y. Yamauchi, *Mater. Chem. Front.*, 2021, 5, 3480–3488.
- 11 L. Han, H. L. Huang, X. B. Fu, J. F. Li, Z. L. Yang, X. J. Liu, L. K. Pan and M. Xu, *Chem. Eng. J.*, 2020, **392**, 123733.
- 12 G. T. Xiang, J. M. Yin, G. M. Qu, P. X. Sun, P. Y. Hou, J. Z. Huang and X. J. Xu, *Inorg. Chem. Front.*, 2019, **6**, 2135–2141.
- 13 Y. Y. Zheng, J. Xu, X. S. Yang, Y. J. Zhang, Y. Y. Shang and X. Y. Hu, *Chem. Eng. J.*, 2018, 333, 111–121.
- 14 P. C. Du, Y. M. Dong, C. Liu, W. L. Wei, D. Liu and P. Liu, *J. Colloid Interface Sci.*, 2018, **88**, 57–68.
- 15 K. H. Han, Y. Liu, H. Huang, Q. H. Gong, Z. L. Zhang and G. W. Zhou, *RSC Adv.*, 2019, **9**, 21608–21615.
- 16 L. Wan, Y. L. Yuan, J. X. Liu, J. Chen, Y. Zhang, C. Du and M. J. Xie, *Electrochim. Acta*, 2021, 368, 137579.
- 17 T. W. Liu, Y. W. Zheng, W. Zhao, L. Cui and J. Q. Liu, J. Colloid Interface Sci., 2019, 556, 743–752.
- 18 L. Wan, Y. L. Yuan, J. X. Liu, J. Chen, Y. Zhang, C. Du and M. J. Xie, *Electrochim. Acta*, 2021, 368, 137579.
- 19 S. Chen, J. W. Zhu, X. D. Wu, Q. F. Han and X. Wang, ACS Nano, 2010, 4, 2822–2830.
- 20 Y. Song, M. J. Shang, J. G. Li and Y. H. Su, Chem. Eng. J., 2021, 405, 127059.
- 21 T. Liu, J. H. Liu, L. Y. Zhang, B. Cheng and J. G. Yu, *J. Mater. Sci. Technol.*, 2020, 47, 113–121.
- 22 Y. F. Zhu, F. F. Wang, H. Zhang, X. Lv, Z. Hu, X. Y. Fan, J. Y. Jia and X. D. Guo, *J. Alloys Compd.*, 2018, **30**, 276–282.
- 23 W. Ge, A. Encinas, M. F. Ruiz and S. X. Song, *J. Energy Storage*, 2020, 31, 101607.
- 24 Q. F. Meng, K. F. Cai, Y. X. Chen and L. D. Chen, *Nano Energy*, 2017, 36, 268–285.
- 25 X. T. Xu, J. Tang, H. Y. Qian, S. J. Hou, Y. Bando, M. S. A. Hossain, L. K. Pan and Y. Yamauchi, *ACS Appl. Mater. Interfaces*, 2017, **9**, 38737–38744.

26 Y. Y. Chen, T. Liu, L. Y. Zhang and J. G. Yu, ACS Sustainable Chem. Eng., 2019, 7, 11157–11165.

- 27 Y. Wang, Z. L. Yin, X. H. Li, H. J. Guo, D. C. Zhang and Z. X. Wang, *Electrochim. Acta*, 2019, **309**, 140–147.
- 28 W. Z. Li, X. H. Zu, Y. X. Zeng, L. Y. Zhang, Z. L. Tang, G. B. Yi, Z. H. Chen, W. J. Lin, X. F. Lin, H. K. Zhou, J. Xiao and Y. L. Deng, *Nano Energy*, 2020, **67**, 104275.
- 29 M. Sakthivel, R. Sukanya, S. M. Chen, K. Pandi and K. C. Ho, *Renewable Energy*, 2019, **138**, 139–151.
- 30 B. Sebastiano, P. Elisa, E. Antonio, C. Nicola, M. G. Beatriz, O. N. Reinier, P. Mirko and B. Francesco, *Adv. Funct. Mater.*, 2019, 29, 1807659.

- 31 R. Q. Yao, H. Shi, W. B. Wan, Z. Wen, X. Y. Lang and Q. Jiang, *Adv. Mater.*, 2020, 32, 1907214.
- 32 H. M. Zhao, Z. P. Zhang, C. G. Zhou and H. F. Zhang, *Appl. Surf. Sci.*, 2021, 541, 48458.
- 33 H. I. Hsiang, C. H. She and S. H. Chung, *Ceram. Int.*, 2021, 47, 25942–25950.
- 34 W. L. Wu, C. H. Zhao, C. W. Wang, T. T. Liu, L. Wang and J. F. Zhu, *Appl. Surf. Sci.*, 2021, **563**, 150324.
- 35 T. T. Bi, J. L. Jiang, Y. Lei, X. Zheng, Z. F. Jia, Z. Q. Wei and H. Yang, *Appl. Surf. Sci.*, 2020, 530, 147317.
- 36 F. L. Zhao, D. Xie, W. X. Huang, X. R. Song, M. A. Z. G. Sial, H. L. Wu, F. Deng, Q. Zhang, J. Z. Zou and X. R. Zeng, J. Colloid Interface Sci., 2020, 580, 160–170.